photonics

MDPI

Article

Joint SOP-Based and Fading-Suppressed Phase-Based Vibration Sensing Integrated in Short-Reach Optical Interconnects

Quhao Zhuo [1,†], Moxuan Luo [1,†], Yuanqing Li [1], Qiuqi Hu [1], Jianwei Tang [2,3], Qi Wu [4], Shuai Qu [4], Bang Yang [3], Zhaopeng Xu [2], Yanfu Yang [3], Jinlong Wei [2,*] and Qiaozhi Lei [1,*]

[1] Education Center of Experiments and Innovations, Harbin Institute of Technology, Shenzhen 518055, China; 24s052008@stu.hit.edu.cn (Q.Z.); 2023311101@stu.hit.edu.cn (M.L.); liyq@hit.edu.cn (Y.L.); huqiuqi@hit.edu.cn (Q.H.)
[2] Pengcheng Laboratory, Shenzhen 518000, China; tangjw@pcl.ac.cn (J.T.); xuzhp@pcl.ac.cn (Z.X.)
[3] School of Information Science and Technology, Harbin Institute of Technology, Shenzhen 518055, China; yangyanfu@hit.edu.cn (Y.Y.)
[4] Photonics Research Institute, The Hong Kong Polytechnic University, Hong Kong SAR, China; polyu-qi.wu@polyu.edu.hk (Q.W.); qushuai@sdlaser.cn (S.Q.)
* Correspondence: weijl01@pcl.ac.cn (J.W.); leiqiaozhi@hit.edu.cn (Q.L.)
† These authors contributed equally to this work.

Abstract

With the advancement of artificial intelligence (AI) technologies such as large language models and autonomous driving, the data traffic via optical interconnects in data centers has surged significantly. The stability of the optical interconnects relies on intelligent operation and maintenance (O&M). Integrated sensing and communication (ISAC) over fibers enables vibration sensing utilizing existing communication fibers, providing critical support for intelligent O&M in data centers. Compared to sensing in the coherent systems, it is difficult to use phase and state of polarization (SOP) monitoring for vibration detection in intensity-modulation and direct-detection (IM-DD) systems. In this paper, we propose a joint phase-based and SOP-based sensing scheme integrated in IM-DD systems. In the proposed scheme, the received IM-DD communication signals are tapped for sensing with a power ratio of 10%. Then the tapped signals are split for vibration sensing based on SOP and phase, respectively. In the phase-based sensing arm, a circulator, a 3×3 coupler and two Faraday rotating mirrors (FRMs) are used to build an unbalanced Michelson interferometer without phase fading and polarization fading. For the purpose of SOP-based sensing, a polarizer is used to monitor the vibration-induced SOP variations. Experimental results demonstrate that the proposed scheme enables vibration sensing based on both phase and SOP across a frequency range of 200 Hz to 10 kHz. Regarding the communication performance, the integration of the sensing system only induces 0.8 dB received optical power penalty. This vibration-sensing scheme based on both phase and SOP can be integrated into pluggable optical modules, providing an efficient and reliable solution for intelligent optical network O&M.

Keywords: integrated sensing and communication; optical fiber communication; intensity-modulation and direct detection; optical network operation and maintenance

Check for updates

Received: 6 May 2026
Revised: 8 June 2026
Accepted: 10 June 2026
Published: 11 June 2026

Copyright: © 2026 by the authors. Licensee MDPI, Basel, Switzerland. This article is an open access article distributed under the terms and conditions of the Creative Commons Attribution (CC BY) license.

1. Introduction

Driven by cloud computing and the distributed training of artificial intelligence (AI) models, communication traffic in data centers has continued to increase [1,2]. Optical cables

serve as the physical foundation of these interconnects, enabling ultra-high-speed and high-capacity data transmission. Despite their stable transmission performance, these cables face significant failure risks from external physical disturbances, including construction damage [3], lightning strikes [4], seismic events [5], as well as cable aging [6]. Reliable operation of large-scale optical interconnects depends on efficient cable monitoring and intelligent operation and maintenance (O&M). However, the cost-effective implementation of these O&M measures remains a critical challenge for the telecommunications industry.

Integrated sensing and communication (ISAC) has emerged as a key solution to the challenge of intelligent O&M [7]. By reusing existing telecommunication fibers to build sensing networks, ISAC provides real-time early warnings of external intrusions and potential cable damage by accurately sensing vibration signatures along the fiber [8,9]. To facilitate practical deployment, current research focuses on achieving cost-effective and endogenous vibration sensing that shares hardware and is highly compatible with existing communication systems [10].

In coherent optical systems, traditional sensing schemes mainly rely on backscattering mechanisms. A typical example is distributed acoustic sensing (DAS) [11,12], which uses Rayleigh scattering to detect and locate fiber vibrations. However, these backscattering schemes are incompatible with multi-span transmission links. To address this, forward-transmission sensing offers a low-cost alternative that is fully compatible with commercial coherent systems. These forward schemes achieve sensing by directly extracting the state of polarization (SOP) and phase information from the optical carrier. For SOP-based sensing schemes, SOP variations are commonly tracked using the polarization demultiplexing module in the receiver's digital signal processing (DSP). Specifically, the SOP can be reconstructed by the tap coefficients of adaptive multiple-input and multiple-output (MIMO) filter [13,14] or frequency-domain pilot tones (FPTs) [15]. For phase-based sensing schemes, vibration-induced phase variations can be extracted directly using carrier phase estimation (CPE) module [7,16]. Schemes based on conventional carrier recovery rely on ultra-narrow-linewidth lasers and are highly sensitive to residual frequency offsets [7]. In ref. [16], a phase-based vibration sensing scheme utilizing FPTs under commercial external-cavity lasers (ECLs) is proposed. Owing to its accurate dynamic frequency offset estimation, this scheme achieves phase-based sensing under commercial lasers. For joint SOP-based and phase-based sensing, existing research has demonstrated continuous phase and SOP joint monitoring over transoceanic submarine cables and long-haul live fiber networks, enabling the sensing of external vibrations such as seismic waves [17]. The authors of ref. [18] compare the performance of SOP-based and phase-based sensing over deployed metro fibers, indicating that SOP-based sensing is more robust to background noise. Despite the maturity of sensing techniques in coherent systems, their heavy reliance on coherent DSP prevents their direct transfer to IM-DD architectures.

In recent years, vibration-sensing schemes integrated in IM-DD systems are mainly based on SOP. To obtain complete SOP information in IM-DD architectures for link-vibration detection, external polarimeters can be employed [19,20]. However, this approach requires additional expensive hardware and has challenges in integration. To ensure cost efficiency and hardware simplicity, SOP sensing in IM-DD systems has shifted toward minimalist architectures based on the extraction of partial polarization features. The scheme proposed in [21] uses a coupler and a polarizer to extract SOP information. However, the integration of this scheme and communication systems has not been demonstrated. A polarization beam splitter (PBS) can be used to obtain the S_0 and S_1 parameters from the communication signal, achieving SOP-based sensing [22]. In ref. [23], 10% of the optical power of the original communication signal was extracted using a coupler for SOP detection. Then, a PBS and two photodetectors (PDs) were used to detect the power variations on two

orthogonal polarization directions. Due to the direct detection of IM-DD systems, the phase information of the optical carrier is difficult to be obtained. Extracting the vibration-induced phase in IM-DD systems remains a fundamental challenge. Existing work [24] proposed introducing an additional local oscillator laser into IM-DD links for optical beating to extract vibration-induced phase for sensing. That inevitably increases the deployment cost of existing IM-DD systems. In our previous work, a phase-fading-free phase-based and SOP-based sensing scheme without a local oscillator laser for IM-DD interconnects was proposed [25]. The scheme employs an unbalanced Mach–Zehnder interferometer to transform phase variations into detectable differential intensity signals. Nevertheless, the rotations of polarization within the interferometer arms lead to polarization fading, causing phase demodulation failure.

To address this fundamental limitation, a joint SOP-based and phase-based sensing scheme compatible with IM-DD systems is proposed. The architecture integrates minimalist SOP-based sensing based on a polarizer and fading-free phase-based sensing. In the phase-based sensing arm, an unbalanced Michelson interferometer incorporating two Faraday rotating mirrors (FRMs) and a 3×3 coupler is used for vibration-induced phase demodulation. The two FRMs guarantee polarization alignment between the returning beams from both interferometric arms, physically suppressing polarization fading without reliance on any polarization controllers. Meanwhile, the 3×3 coupler configuration introduces an intrinsic $2\pi/3$ inter-port phase difference and simultaneously suppresses phase fading in phase demodulation. Both fading mechanisms are thus suppressed at the physical level, without extra complex DSP sensing.

The paper is organized as follows: In Section 2, the principles of the proposed joint SOP-based and phase-based vibration sensing scheme are introduced. In Section 3, we describe the experimental setup of the proposed scheme integrated in an IM-DD system. In Section 4, we present and discuss the experimental results, including vibration sensing performance based on SOP and phase, as well as the communication performance with sensing integration. Finally, conclusions are drawn in Section 5.

2. Principles

External disturbances induce mechanical vibrations in fiber links. These vibrations modulate the phase and SOP of the signal through the variations in structures of fiber. To detect these vibrations, a small fraction of the received optical power is tapped for sensing. The proposed scheme has only a slight impact on communication performance while enabling reliable vibration detection through both SOP-based and phase-based demodulation. Notably, the phase-sensing architecture physically suppresses both polarization fading and phase fading by using a 3×3 coupler and FRMs. This section details the vibration-demodulation principles employed in the system.

2.1. SOP-Based Sensing

The principle of SOP-based vibration demodulation is illustrated in Figure 1a. External vibrations induce stress asymmetry and alter the refractive-index distribution of the fiber. This change creates stress-induced birefringence. Consequently, the SOP of the link evolves rapidly. At the receiver side, the optical signal passes through a polarizer and is detected by a PD. To suppress additive noise, a sliding window is used to perform time-domain averaging on the received signal $I_1(t)$. The low-frequency sensing signal detected by PD_1 can be expressed as [26]:

$$I_1(t) = C(t)\cos^2[\theta_{\mathrm{Vib}}(t)] \otimes h(t) = C\cos^2[\theta_{\mathrm{Vib}}(t)]. \quad (1)$$

Here, $C(t)$ denotes the optical power measured directly by PD_1 in the SOP sensing branch. $\theta_{Vib}(t)$ denotes the angle between the SOP and the polarizer axis. $h(t)$ denotes the impulse response of the narrow-bandwidth PD used in the experiment. The bandwidth of the PD is significantly lower than the baud rate of the communication signal. Consequently, its low-pass filtering effect removes the fluctuations of high-frequency power, and only the time-averaged optical power C is retained [25]. Since the frequency of the mechanical vibrations is much lower than the detection bandwidth of the PD, the sensing features carried by the SOP are preserved.

In the optical signal detected by the PD, the alternating-current (AC) component of $I_1(t)$ denoted by $\widetilde{I}_1(t)$, can be expressed as

$$\widetilde{I}_1(t) = \frac{1}{2} C \cos[2\theta_{Vib}(t)]. \tag{2}$$

Finally, $\theta_{Vib}(t)$ is estimated through an arccosine operation. Subsequent time differentiation yields the SOP angular velocity, $\omega_{Vib}(t)$, as defined in Equation (3).

$$\omega_{Vib}(t) = \frac{d}{dt}\left\{\frac{1}{2}\arccos\left[\frac{2\widetilde{I}_1(t)}{C}\right]\right\}. \tag{3}$$

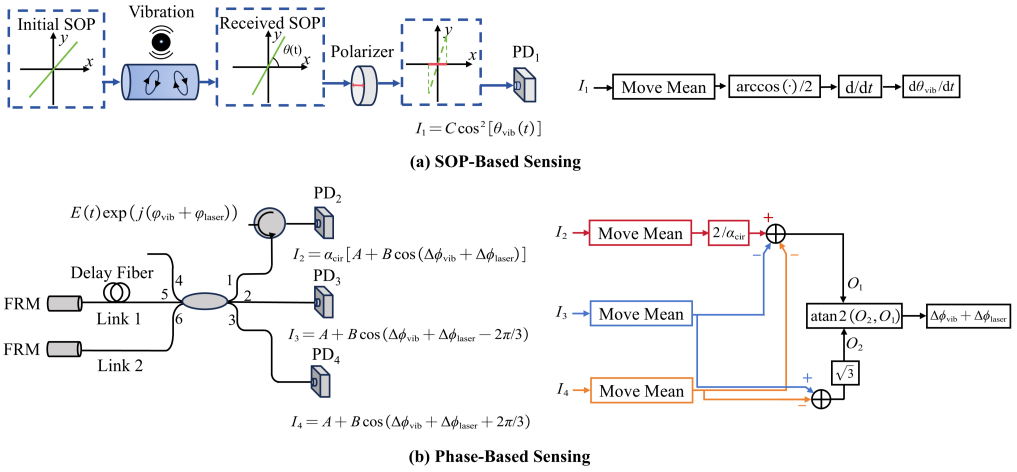


Figure 1. The principles of the proposed simultaneous SOP-based and phase-based vibration sensing scheme. (**a**) The schematic of SOP-based vibration sensing. (**b**) The schematic of the phase-based vibration sensing.

The differentiation operation offers two key advantages. First, it captures high-frequency dynamic vibration features. Second, it effectively suppresses slow SOP drifts caused by ambient temperature fluctuations or gradual stress variations. Since the arccosine function is defined over $[0, \pi]$, the recovered angle is subject to inherent sign ambiguity. Nevertheless, as the proposed scheme targets vibration detection rather than precise SOP reconstruction, this limitation does not affect the sensing functionality. Although pre-measuring the input optical power C of the SOP sensing branch enables SOP angle demodulation, laser power drift and vibration-induced fiber transmission loss variations may cause optical power fluctuations in practice. To address this issue, an additional tap coupler can be introduced into the SOP sensing branch to monitor the input optical power in real time, thereby avoiding SOP demodulation errors induced by optical power fluctuations.

The proposed SOP-vibration demodulation scheme requires only a polarizer and a single PD, ensuring low hardware complexity. This makes it highly compatible with cost-sensitive IM-DD systems. Notably, the single polarizer–PD combination has inherent

limitations. The detected intensity is proportional to $I = \frac{1}{2}(S_0 + S_1)$, meaning only the S_1 component of the Stokes vector is captured. SOP variations corresponding to changes in S_2 and S_3 therefore cannot be detected. In addition, the sensitivity vanishes near $\theta = 0^\circ$ and $\theta = 90^\circ$, leading to sensitivity fading at these operating points. To achieve fading-suppressed SOP demodulation, full Stokes parameter measurement is required, necessitating at least four PDs as in a Stokes receiver [27] or a polarimeter [19]. This would significantly increase hardware complexity and cost. Therefore, the single polarizer–PD configuration represents a deliberate design trade-off in favor of low-cost and low-complexity deployment.

2.2. Phase-Based Sensing

The principle of phase-based vibration demodulation is illustrated in Figure 1b. This branch employs an unbalanced Michelson interferometer based on a 3×3 coupler to achieve phase demodulation with phase-fading-suppressed [28]. In addition, FRMs are incorporated into the phase-sensing structure to suppress polarization fading. At the receiver side, the optical field carrying the vibration-induced phase can be expressed as

$$E_{\text{phase}}(t) = E(t)e^{j[\phi_{\text{Vib}}(t)+\phi_{\text{Laser}}(t)]}. \tag{4}$$

Here, $\phi_{\text{Vib}}(t)$ denotes the phase variation induced by vibration along the fiber link, and $\phi_{\text{Laser}}(t)$ denotes the laser phase noise. The sensing optical signal enters port #1 of the circulator and exits from port #2. It then enters port #1 of the 3×3 coupler, where the optical field can be expressed as

$$E_1(t) = \sqrt{\alpha_{\text{Cir}}}E(t)e^{j[\phi_{\text{Vib}}(t)+\phi_{\text{Laser}}(t)]}. \tag{5}$$

In Equation (5), α_{Cir} represents the insertion loss of the circulator in terms of optical power. The 3×3 coupler subsequently splits the optical beam into three paths. Neglecting the insertion loss of the coupler, the optical fields output from ports #5 and #6 into the interferometric arms are denoted by $E_5(t)$ and $E_6(t)$ as [29]

$$E_{5,6}(t) = \frac{\sqrt{3}}{3}\sqrt{\alpha_{\text{Cir}}}E(t)e^{j[\phi_{\text{Vib}}(t)+\phi_{\text{Laser}}(t)]}. \tag{6}$$

These fields then propagate through two separate interferometric arms. Specifically, Link 1 connects port #5 to an FRM through a delay fiber with a delay of τ. Meanwhile, Link 2 connects port #6 directly to another FRM. After reflections by the FRMs, both beams return to the 3×3 coupler and interfere with each other. The resulting optical fields, $E_5'(t)$ and $E_6'(t)$, can be expressed as follows:

$$E_5'(t) = \frac{\sqrt{3}}{3}\sqrt{\alpha_{\text{Cir}}}E(t)e^{j[\phi_{\text{Vib}}(t)+\phi_{\text{Laser}}(t)]} \tag{7}$$

$$E_6'(t) = \frac{\sqrt{3}}{3}\sqrt{\alpha_{\text{Cir}}}E(t+\tau)e^{j[\phi_{\text{Vib}}(t+\tau)+\phi_{\text{Laser}}(t+\tau)]}. \tag{8}$$

The phase-sensing structure in [25] employs an unbalanced Mach–Zehnder interferometer. This setup relies on a polarization controller to align the polarization states of the two interfering beams. However, SOP drift and manual adjustment errors prevent perfect polarization alignment, thereby inducing polarization fading. Such polarization fading reduces fringe visibility and degrades demodulation performance. In contrast, the proposed scheme uses FRMs to eliminate polarization fading caused by slow SOP variations, thereby improving the robustness of phase demodulation.

The principle of phase demodulation without polarization fading is analyzed below. Assuming lossless FRMs and fiber, the delay fiber is treated as a reciprocal linear birefringent medium. For Link 1, the forward and backward Jones matrices of the delay fiber are denoted by $\mathbf{J}_{\mathrm{L}}$ and $\mathbf{J}_{\mathrm{L}}^{\mathrm{T}}$, respectively. An FRM consists of a 45° Faraday rotator and a fiber reflector. Neglecting insertion loss, its round-trip Jones matrix, $\mathbf{R}_{\mathrm{FRM}}$, is expressed as [30]

$$\mathbf{R}_{\mathrm{FRM}} = \begin{bmatrix} 0 & -1 \\ 1 & 0 \end{bmatrix}. \tag{9}$$

Therefore, the round-trip Jones matrix of the beam propagating through Link 1 and the FRM, denoted by $\mathbf{J}_{\mathrm{RT}}$, can be written as

$$\mathbf{J}_{\mathrm{RT}} = \mathbf{J}_{\mathrm{L}}^{T}\mathbf{R}_{\mathrm{FRM}}\mathbf{J}_{\mathrm{L}} = \det(\mathbf{J}_{\mathrm{L}}) \begin{bmatrix} 0 & -1 \\ 1 & 0 \end{bmatrix} = e^{j\varphi} \begin{bmatrix} 0 & -1 \\ 1 & 0 \end{bmatrix}. \tag{10}$$

Here, φ denotes the additional phase accumulated during the round trip through the FRM. This derivation demonstrates that the round-trip Jones matrix $\mathbf{J}_{\mathrm{RT}}$ of Link 1 is independent of the Jones matrix of the delay fiber, $\mathbf{J}_{\mathrm{L}}$. Consequently, the polarization states of the returning beams from both interferometric arms remain aligned. This alignment effectively suppresses polarization fading and significantly enhances the interference effect under slowly varying polarization conditions.

When the returning beams re-enter an ideal, symmetric, and lossless 3×3 coupler and interfere, fixed phase shifts of $2\pi/3$ are introduced at the three output ports. The output light from port #1 is sent through the circulator to PD_2, while the output light from ports #2 and #3 is detected directly by PD_3 and PD_4, respectively. After additive noise in the PD signals is suppressed by sliding averaging, the three detected intensities can be expressed as follows [29]:

$$I_2(t) = \alpha_{\mathrm{Cir}}\{A(t) + B(t)\cos[\Delta\phi_{\mathrm{Vib}}(t) + \Delta\phi_{\mathrm{Laser}}(t)]\} \otimes h(t), \tag{11a}$$

$$I_3(t) = \left\{A(t) + B(t)\cos\left[\Delta\phi_{\mathrm{Vib}}(t) + \Delta\phi_{\mathrm{Laser}}(t) + \frac{4\pi}{3}\right]\right\} \otimes h(t), \tag{11b}$$

$$I_4(t) = \left\{A(t) + B(t)\cos\left[\Delta\phi_{\mathrm{Vib}}(t) + \Delta\phi_{\mathrm{Laser}}(t) + \frac{2\pi}{3}\right]\right\} \otimes h(t). \tag{11c}$$

Here, $\Delta\phi_{\mathrm{Vib}}(t) = \phi_{\mathrm{Vib}}(t+\tau) - \phi_{\mathrm{Vib}}(t)$ represents the delay-differential vibration-induced phase. Similarly, $\Delta\phi_{\mathrm{Laser}}(t) = \phi_{\mathrm{Laser}}(t+\tau) - \phi_{\mathrm{Laser}}(t)$ denotes the delay-differential laser phase noise. The parameters $A(t)$ and $B(t)$ represent the detected signal intensity and the intensity of the interference term, respectively. This differential structure converts the transient phase evolution into detectable intensity variations. Considering the low-pass filtering effect of the PDs, the following expressions are obtained:

$$A = A(t) \otimes h(t) \tag{12}$$

$$B = B(t) \otimes h(t). \tag{13}$$

where A and B denote the average detected signal intensity and the average interference-term intensity, respectively. Accordingly, the three interference signals for phase-based sensing can be rewritten as

$$I_2(t) = \alpha_{\mathrm{Cir}}\{A + B\cos[\Delta\phi_{\mathrm{Vib}}(t) + \Delta\phi_{\mathrm{Laser}}(t)]\}, \tag{14a}$$

$$I_3(t) = A + B\cos\left[\Delta\phi_{\mathrm{Vib}}(t) + \Delta\phi_{\mathrm{Laser}}(t) + \frac{4\pi}{3}\right], \tag{14b}$$

$$I_4(t) = A + B\cos\left[\Delta\phi_{\mathrm{Vib}}(t) + \Delta\phi_{\mathrm{Laser}}(t) + \frac{2\pi}{3}\right]. \tag{14c}$$

The inherent $2\pi/3$ phase difference ensures that at least one PD remains in a high-sensitivity detection region at any given phase angle. This mechanism also ensures that at least two of the three interference outputs maintain non-zero intensity at any given time. By effectively suppressing phase fading, it fundamentally enhances the robustness of the phase-demodulation process. To reconstruct the vibration-induced phase, we employ the arctangent algorithm [31]. First, the circulator loss in I_2 is compensated. Subsequently, the tangent of the differential vibration-induced phase is reconstructed using linear combinations of the three signals [31]:

$$O_1 = \frac{2I_2(t)}{\alpha_{\mathrm{Cir}}} - I_3(t) - I_4(t) = 3B\cos[\Delta\phi_{\mathrm{Vib}}(t) + \Delta\phi_{\mathrm{Laser}}(t)], \tag{15}$$

$$O_2 = \sqrt{3}[I_3(t) - I_4(t)] = 3B\sin[\Delta\phi_{\mathrm{Vib}}(t) + \Delta\phi_{\mathrm{Laser}}(t)]. \tag{16}$$

The ratio O_2/O_1 eliminates both the DC component A and the interference amplitude fluctuations B. Subsequently, the differential vibration phase is directly demodulated via a two-argument arctangent operation:

$$\mathrm{atan2}\left(O_2,\ O_1\right) = \Delta\phi_{\mathrm{Vib}}(t) + \Delta\phi_{\mathrm{Laser}}(t). \tag{17}$$

Compared with the differential cross-multiplication (DCM) algorithm [29], the arctangent algorithm significantly reduces the number of multiplication and differentiation operations. This reduction lowers computational complexity and eliminates numerical noise introduced by differentiation. Furthermore, the arctangent algorithm exhibits strong robustness against random optical power fluctuations. By integrating FRMs and a 3×3 coupler, the proposed architecture achieves robust vibration-phase demodulation by suppressing both phase fading and polarization fading. Notably, the proposed phase-based sensing scheme is fully compatible with IM-DD systems while maintaining low hardware complexity.

3. Experimental Setup

Figure 2 illustrates the experimental setup of the proposed joint phase-based and SOP-based vibration-sensing scheme. This architecture is fully compatible with IM-DD communication systems. At the transmitter side, a pseudorandom binary sequence (PRBS) is generated and mapped into a 64-Gbaud four-level pulse-amplitude modulation (PAM-4) signal. Then, a root-raised-cosine (RRC) filter with a roll-off factor of 0.05 is applied to perform Nyquist shaping. Finally, the data stream is upsampled and loaded into an arbitrary waveform generator (AWG, 8199A, Keysight Technologies, Santa Rosa, CA, USA) operating at 128 GSa/s. The optical carrier is provided by an external-cavity laser (ECL, PHX-C-F-M-C34, Shenzhen Photonx Technology Co., Ltd., Shenzhen, China) with an output power of 16 dBm and a nominal linewidth of 3 kHz. A Mach–Zehnder modulator (MZM), driven by the AWG, performs intensity modulation. The signal is then transmitted through a 1 km standard single-mode fiber (SSMF). To quantitatively evaluate the sensing performance, a piezoelectric transducer (PZT) is inserted in series with the fiber link to emulate vibrations at various frequencies. At the receiver side, the optical signal passes through a variable optical attenuator (VOA) to regulate the received optical power (ROP). Subsequently, an optical coupler splits the signal, allocating 10% of the power to vibration sensing and the remaining 90% to high-speed communication.

In the sensing branch, the tapped sensing optical signal is split by an optical coupler with a 50/50 power ratio and then fed into the phase-sensing and SOP-sensing branches. In the SOP-based sensing branch, the optical signal passes through a polarizer and is then directly detected by a PD. In the phase-based sensing branch, the optical signal

enters port #1 of a 3 × 3 coupler via a circulator. The coupler splits the light into a delay arm (Link 1) and a reference arm (Link 2). The optical signal from port #5 propagates through the 2 m delay fiber in Link 1, is reflected by FRM 1, and undergoes a round trip back to the same port. Simultaneously, the signal from port #6 is directly reflected by FRM 2 in Link 2. Upon returning to the 3 × 3 coupler, these two beams interfere. The polarization of the interfering beams remains aligned, effectively suppressing polarization fading. The interference optical signals from ports #2 and #3 are directly detected by PD_3 and PD_4, respectively. Meanwhile, the signal from port #1 is directed back through the circulator to PD_2. The insertion loss of the circulator from port #2 to port #3, denoted as α_{Cir}, was measured to be 0.7 dB. The four PDs utilized in the sensing branch have a uniform bandwidth of 5 MHz. Including the SOP-sensing signal from PD_1, all four electrical outputs of PDs are recorded by a real-time oscilloscope (RTO, DSOX2014A, Keysight Technologies, Santa Rosa, CA, USA) at a sampling rate of 2.5 MSa/s. Finally, a 20-point sliding window average is applied to the signals to suppress background noise.

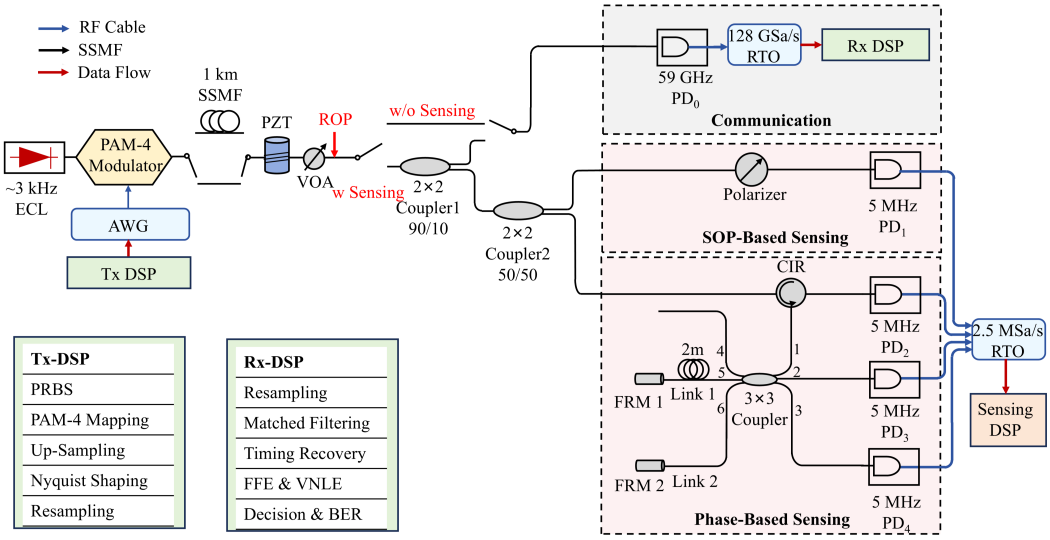


Figure 2. Experimental setup of the proposed phase-based and SOP-based vibration sensing scheme integrated in IM-DD systems. The blue line represents the RF cable. The black line represents the SSMF. The red line represents the data flow. SSMF, standard single-model fiber; RF, radio frequency; AWG, arbitrary waveform generator; DSP, digital signal processing; PZT, piezoelectric transducer; VOA, variable optical attenuator; CIR, circulator; RTO, real-time sampling oscilloscope; FFE, feed-forward equalizer; VNLE, Volterra nonlinear equalizer; BER, bit error rate.

The selection of delay fiber length represents a critical trade-off in the phase-based sensing branch. An excessively long delay fiber introduces substantial laser phase noise over the delay interval, degrading demodulation accuracy. An excessively short delay fiber yields an insufficiently small differential vibration phase, limiting detection sensitivity. Therefore, the delay fiber length must be carefully optimized according to the laser linewidth, the target sensing frequency range, and the required detection sensitivity. It is further worth noting that the demodulated differential vibration phase inevitably contains the differential laser phase noise.

The impact of laser phase noise is closely related to the laser linewidth. When the laser linewidth is excessively large, the accumulated phase noise becomes dominant, submerging the differential vibration phase and degrading demodulation accuracy. Moreover, broader-linewidth lasers exhibit more pronounced phase noise at low Fourier frequencies, which correspondingly elevates the effective lower frequency bound of phase-based sensing and compresses the usable sensing bandwidth. Therefore, when extending the proposed

scheme to broader-linewidth laser systems, a shorter delay fiber should be adopted to mitigate the accumulated laser phase noise, albeit at the cost of reduced sensing sensitivity.

At the receiver side, the communication signal is detected by a 59-GHz high-speed PD (Finisar, XPDV2320, Finisar Corporation, Sunnyvale, CA, USA). The resulting electrical signal is captured by an RTO (UXR0594AP, Keysight Technologies, Santa Rosa, CA, USA) at a sampling rate of 128 GSa/s. In the offline DSP flow, the data are first resampled to two samples per symbol (SPS). Matched filtering is then performed using the same RRC filter. A timing-recovery module is introduced to correct the clock offset between the transmitter and receiver [32]. To mitigate intersymbol interference (ISI), a feed-forward equalizer (FFE) with 99 taps is employed. Furthermore, a Volterra nonlinear equalizer (VNLE) is utilized to compensate for nonlinearities originating from the modulator and square-law detection [33]. Finally, the bit error rate (BER) is calculated after a hard-decision process.

4. Experimental Results and Discussions

4.1. Sensing Results

First, we evaluated the low-frequency vibration-sensing performance of the joint SOP-based and phase-based system. Vibrations at 200, 400, and 600 Hz were applied to the fiber link through the PZT, with the driving voltage set to 10 V_{pp} and the ROP fixed at 0 dBm. The recovered SOP-based sensing waveforms and spectra are illustrated in Figure 3, while the corresponding phase-based results are presented in Figure 4. As shown, the time-domain waveforms reconstructed by both schemes fluctuate at the corresponding vibration frequencies. Furthermore, the spectra exhibit sharp peaks at the target frequencies, with signal-to-noise ratios (SNRs) exceeding 19 dB, confirming the effectiveness of both demodulation schemes for low-frequency vibration detection. By comparing the vibration waveforms obtained from the two demodulation schemes, it can be observed that the waveform demodulated by the SOP-based method resembles a square wave. This phenomenon stems from the irregular fiber winding and twisting on the PZT surface. When vibration is applied, the SOP evolves stochastically across the Poincaré sphere due to the random birefringence effect. However, the polarizer–PD combination only captures the intensity fluctuations projected onto the polarizer transmission axis. This projection mechanism introduces nonlinear distortion into the demodulated sensing signal. A comparison of the spectra obtained from the two demodulation schemes further shows that, for the 200 Hz low-frequency vibration signal, the SNR of the SOP-based sensing scheme is 24 dB higher than that of the phase-based sensing scheme. This difference is mainly due to the extremely small differential phase induced by low-frequency vibration. For a sinusoidal vibration at frequency f, the vibration-induced phase is $\phi_{\mathrm{Vib}}(t) = \Phi_0 \sin(2\pi f t)$. When τ is sufficiently small, the differential phase amplitude is approximated as $|\Delta\phi_{\mathrm{Vib}}| = |\phi_{\mathrm{Vib}}(t+\tau) - \phi_{\mathrm{Vib}}(t)| \approx 2\pi f \tau \Phi_0$. At low vibration frequencies, $|\Delta\phi_{\mathrm{Vib}}|$ becomes extremely small and suffers significant degradation from the laser phase noise. In contrast, the SOP-based demodulation mechanism is inherently immune to phase noise.

Second, the high-frequency sensing performance of the joint SOP-based and phase-based sensing system was evaluated. Vibrations at 6 kHz, 8 kHz, and 10 kHz were applied to the optical link. The SOP-based high-frequency vibration sensing waveforms and spectra are shown in Figure 5, while the phase-based sensing results are presented in Figure 6. As illustrated in the figures, both demodulation schemes are capable of recovering high-frequency vibrations below 10 kHz. The analysis of the spectra demodulated from the two schemes shows that the sensing SNRs are over 40 dB. The experimental results demonstrate the superior performance of the proposed joint SOP-based and phase-based sensing scheme for broadband vibration detection. The demodulated phase-sensing waveforms deviate from an ideal sinusoidal profile. This discrepancy stems from several hardware non-

idealities within the experimental setup. First, the PZT exhibits a nonlinear response to the driving voltage. This response distorts the induced phase fluctuations. Second, the intrinsic phase shifts in the 3×3 coupler deviate from the ideal $2\pi/3$ value. Finally, the FRMs and PDs show inconsistent losses and responsivities. These factors collectively contribute to the waveform distortion.

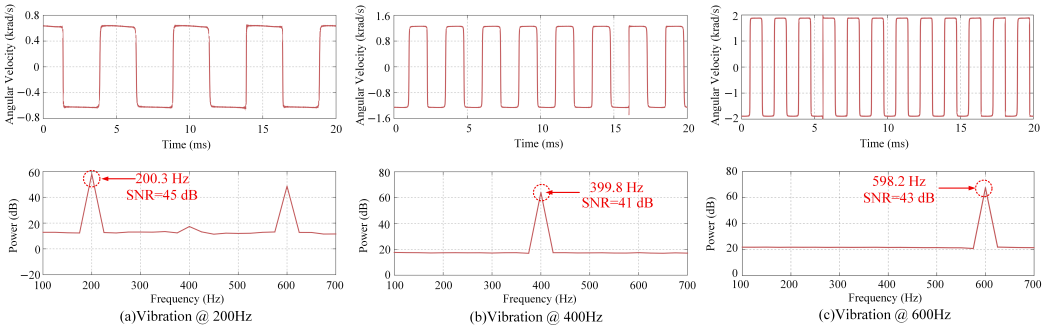


Figure 3. SOP-based sensing waveforms and their corresponding spectra under low-frequency vibrations of 200 Hz (**a**), 400 Hz (**b**) and 600 Hz (**c**).

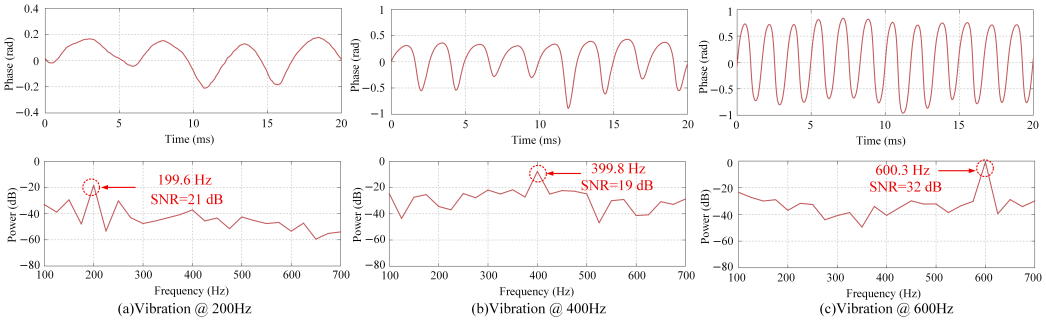


Figure 4. Phase-based sensing waveforms and corresponding spectra under low-frequency vibrations of 200 Hz (**a**), 400 Hz (**b**) and 600 Hz (**c**).

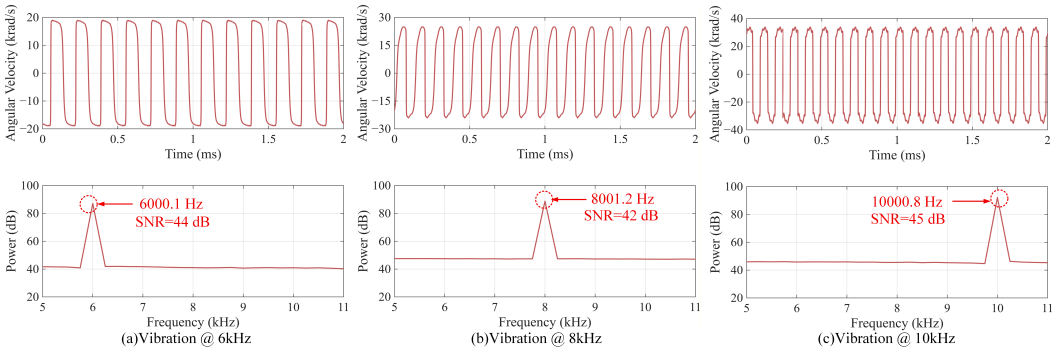


Figure 5. SOP-based sensing waveforms and corresponding spectra under high-frequency vibrations of 6 kHz (**a**), 8 kHz (**b**) and 10 kHz (**c**).

Third, to further characterize the noise floor of the proposed joint SOP-based and phase-based sensing scheme, the background noise was evaluated in the absence of any applied vibration. The recovered SOP-based and phase-based sensing waveforms and their corresponding spectra are shown in Figure 7a and 7b, respectively. As illustrated, the SOP-based sensing channel maintains a flat noise floor across 0 to 10 kHz. Unlike the SOP-based channel, the phase-based sensing channel exhibits a more pronounced noise floor at lower frequencies. This is attributed to the increased phase noise present in the low-frequency region.

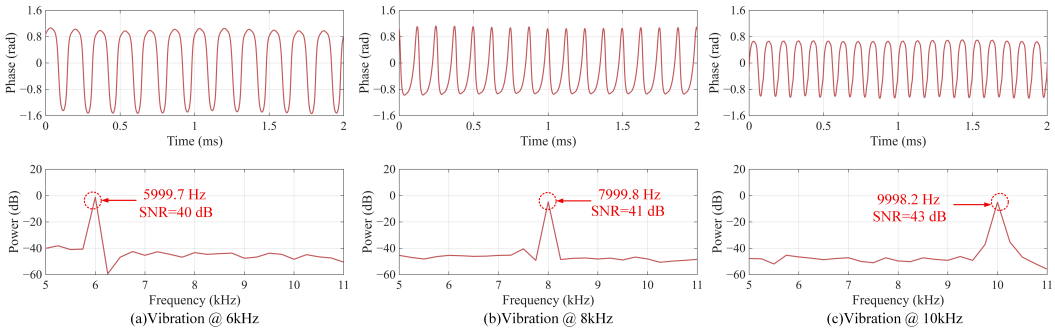


Figure 6. Phase-based sensing waveforms and corresponding spectra under high-frequency vibrations of 6 kHz (**a**), 8 kHz (**b**) and 10 kHz (**c**).

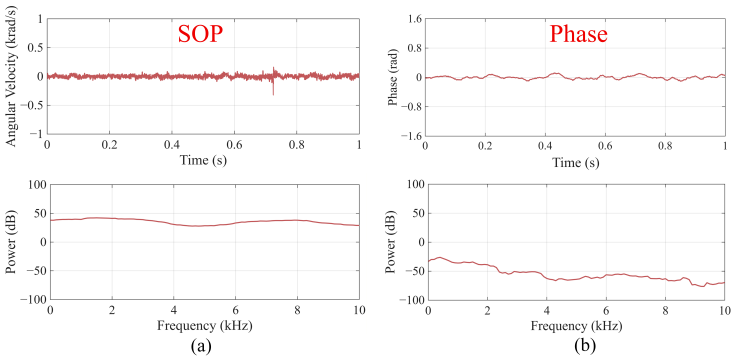


Figure 7. Sensing waveforms and corresponding spectra under background noise conditions. (**a**) SOP-based sensing results. (**b**) Phase-based sensing results.

Then, a frequency-modulated continuous wave (FMCW) vibration with a repetition frequency of 200 Hz and a frequency sweep range from 200 Hz to 10 kHz was applied to the link to verify the capability of the proposed joint SOP-based and phase-based sensing scheme for detecting continuously frequency-varying vibrations. The extracted SOP and phase waveforms are shown in Figure 8a, and the corresponding short-time Fourier transform (STFT) spectra are presented in Figure 8b and 8c, respectively. As shown, the frequencies of both the extracted SOP and phase vary periodically with a period of 5 ms, in good agreement with the applied FMCW vibration. It is worth noting that the STFT spectrum of the extracted phase shows relatively degraded performance at low frequencies. This is primarily due to the low-frequency laser phase noise, which fundamentally limits the SNR of phase-based sensing at low vibration frequencies. In contrast, the SOP-based sensing scheme is inherently insensitive to laser phase noise and therefore maintains better performance at low vibration frequencies. These results further confirm the broadband vibration sensing capability of the proposed scheme, covering a frequency range from 200 Hz to 10 kHz based on both SOP and phase.

Finally, the extracted phase amplitudes under different driving voltage amplitudes were investigated at a vibration frequency of 500 Hz, as shown in Figure 9. Since the SOP-based sensing system does not constitute a classical linear sensing system, the linearity analysis is performed exclusively for the phase-based sensing scheme. The slope of the fitted line indicates a sensor responsivity of 0.0484 rad/V. The obtained coefficient of determination ($R^2 = 0.9972$) demonstrates the satisfactory linear response of the proposed sensing scheme. The error bars represent the standard deviation of ten repeated measurements at each driving voltage, with a maximum value of 0.0318 rad, confirming the repeatability and stability of the proposed system.

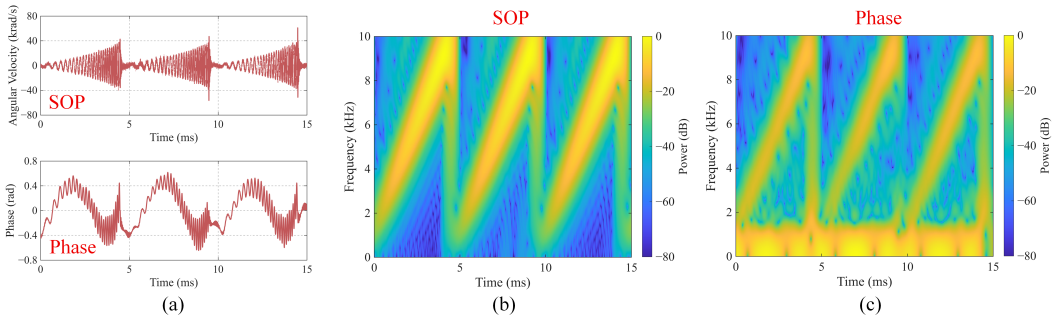


Figure 8. Extracted SOP and phase under FMCW vibration. (**a**) Vibration waveforms of the extracted SOP and phase in the time domain. (**b**) STFT spectrum of the extracted FMCW vibration-induced SOP variation. (**c**) STFT spectrum of the extracted FMCW vibration-induced phase.

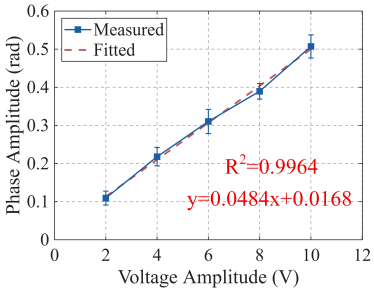


Figure 9. Extracted phase amplitudes for different voltage amplitudes applied to the PZT.

For vibration localization in forward sensing, two approaches are available. In a bidirectional transmission configuration, synchronized receivers are deployed at both ends of the link, and the vibration position is determined through time-of-flight analysis [7,34]. For unidirectional transmission scenarios, localization can be achieved through mode-division multiplexing-based methods [35]. The proposed sensing scheme is compatible with both approaches and provides the underlying sensing foundation for such localization capabilities.

In this work, the SOP-based and phase-based sensing results are presented separately to characterize the individual performance of each modality. The experimental results show that SOP-based sensing achieves higher SNR at low vibration frequencies due to its immunity to laser phase noise, while phase-based sensing more directly reflects the actual vibration amplitude. The complementary characteristics of the two channels provide a solid foundation for future fusion-based vibration event classification.

4.2. Communication Results

The impact of the sensing branch on communication performance was evaluated under both back-to-back (B2B) and 1 km SSMF transmission conditions. Figure 10a compares the BER performances of the systems with and without the sensing branch under B2B conditions. At an ROP of −1 dBm, the constellation diagrams in Figure 10b,c remain highly similar. Near the 7% overhead hard-decision forward-error-correction (HD-FEC) threshold, introducing the sensing branch results in an ROP penalty of only 0.8 dB under B2B conditions. Figure 11a presents the BER performance after 1 km SSMF transmission and the ROP penalty increases slightly to 1.2 dB near the HD-FEC threshold. The corresponding constellation diagrams at ROP = −1 dBm are shown in Figure 11b,c. The ROP penalty originates from the insertion loss of the coupler and the 10% power-tapping loss. These results demonstrate that the joint sensing architecture maintains compatibility with high-speed communication over practical transmission distances with only slight performance degradation.

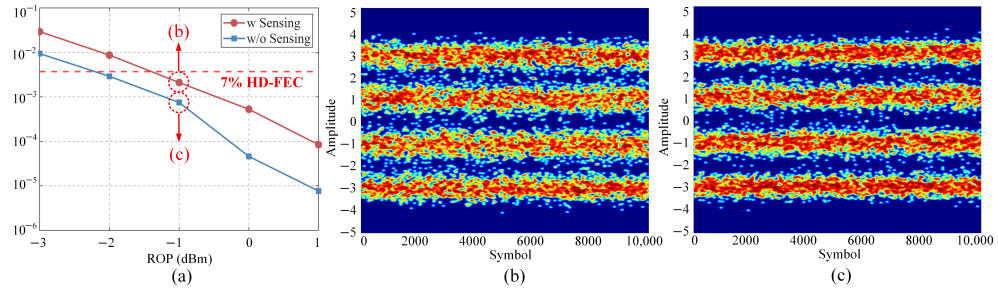


Figure 10. B2B communication performance of the integrated sensing system. (**a**) BER curves of the system with and without the sensing branch under different ROP conditions. Communication signal constellation diagrams at ROP = −1 dBm: with the sensing branch (**b**) and without the sensing branch (**c**).

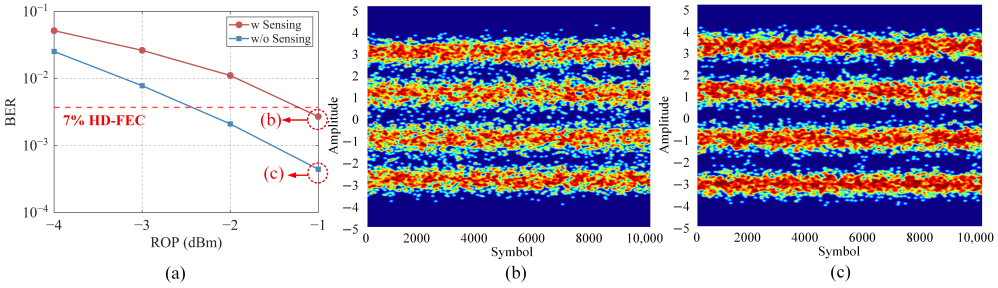


Figure 11. Communication performance of the integrated sensing system after 1 km SSMF transmission. (**a**) BER curves of the system with and without the sensing branch under different ROP conditions. Communication signal constellation diagrams at ROP = −1 dBm: with the sensing branch (**b**) and without the sensing branch (**c**).

5. Conclusions

In summary, a joint SOP-based and phase-based vibration sensing scheme compatible with IM-DD systems is proposed and experimentally validated in this work. In this architecture, 10% of the received optical power is tapped by an optical coupler as a sensing probe. The sensing light is then split equally into two paths. In the first path, a polarizer is used for simplified SOP-variation sensing. In the second path, a 3 × 3 coupler and FRMs are employed to build an unbalanced Michelson interferometer for phase demodulation. This integrated scheme ensures suppression of both phase fading and polarization fading in phase-based sensing. Accurate vibration sensing from 200 Hz to 10 kHz is demonstrated at an ROP of 0 dBm based on both SOP and phase. Furthermore, the integrated sensing and communication system is evaluated using 64 Gbaud PAM-4 signals. Only a 0.8 dB ROP penalty is introduced by the sensing branch near the 7% HD-FEC threshold. This highly integrated, dual-parameter sensing scheme is expected to lay a solid foundation for future multimodal sensing. The proposed scheme offers a promising route toward intelligent O&M in next-generation optical interconnect infrastructures.

Author Contributions: Conceptualization, Q.Z. and M.L.; project administration and supervision, J.W. and Q.L.; experiments, Q.Z., M.L., Y.L., Q.H. and J.T.; writing—original draft preparation, Q.Z. and M.L.; writing—editing, Q.Z. and M.L.; writing—review, Q.W., S.Q., B.Y., Z.X. and Y.Y. All authors have read and agreed to the published version of the manuscript.

Funding: Shenzhen Science and Technology Innovation Commission (JCYJ20250604145259048, JCYJ20240813104835048, KJZD20240903100014019, KJZD20240903100009013), Guangdong Basic and Applied Basic Research Foundation (2025A1515010277), Mobile Information Networks-National Science and Technology Major Project of China (2026ZD1308000), Major Key Project of PCL (PCL2025A01), National Natural Science Foundation of China (62501328), National Talent Program.

Institutional Review Board Statement: Not applicable.

Informed Consent Statement: Not applicable.

Data Availability Statement: Dataset available on request from the authors. The raw data supporting the conclusions of this article will be made available by the authors on request.

Conflicts of Interest: The authors declare no conflicts of interest.

References

1. Saber, M.G.; Jiang, Z. Physical Layer Standardization for AI Data Centers: Challenges, Progress, and Perspectives. *IEEE Netw.* **2026**, *40*, 147–155. [CrossRef]
2. Winzer, P.J. The future of communications is massively parallel. *J. Opt. Commun. Netw.* **2023**, *15*, 783–787. [CrossRef]
3. Wang, Z.; Yang, H.; Li, Y.; Yao, Q.; Yu, T.; Zhang, C.; Liu, W.; Lin, W.; Zhang, J.; Liu, Y.; et al. Co-route fiber recognition and status diagnosis based on integrated sensing and communication in 6G transport networks. *IEEE Internet Things J.* **2024**, *11*, 29348–29359. [CrossRef]
4. Hu, K.; Tong, F.; Lian, W.; Li, W. Model and experimental verification of SOP transient in OPGW based on direct strike lightning. *Opt. Express* **2023**, *31*, 39102–39120. [CrossRef] [PubMed]
5. Carver, C.J.; Zhou, X. Polarization sensing of network health and seismic activity over a live terrestrial fiber-optic cable. *Commun. Eng.* **2024**, *3*, 91. [CrossRef]
6. Wang, T.; Huang, M.F.; Han, S.; Narisetty, C. Employing Fiber Sensing and On-Premise AI Solutions for Cable Safety Protection over Telecom Infrastructure. In Proceedings of the 2022 Optical Fiber Communications Conference and Exhibition (OFC), San Diego, CA, USA, 6–10 March 2022; pp. 1–3.
7. Ip , E.; Huang, Y.K.; Wellbrock, G.; Xia, T.; Huang, M.F.; Wang, T.; Aono, Y. Vibration detection and localization using modified digital coherent telecom transponders. *J. Light. Technol.* **2022**, *40*, 1472–1482. [CrossRef]
8. Guerrier, S.; Dorize, C.; Abdelli, K.; Mardoyan, H.; Pavani, H.; Antonelli, C.; Mecozzi, A.; Koubaa, A.; Darwish, K.; Biyahi, M.; et al. Distributed Coherent Sensing Over Deployed Fibers for Network as a Sensor Applications. *J. Light. Technol.* **2025**, *43*, 1736–1745. [CrossRef]
9. Li, Y.; Li, C.; Liu, Z.; Zhang, T.; Liu, S.; Ge, D.; You, Y.; Zhang, J.; Wang, D.; Zhao, Y.; et al. Research and Experiment on AI-based Co-cable and Co-trench Optical Fibre Detection. In Proceedings of the 2022 European Conference on Optical Communication (ECOC), Basel, Switzerland, 18–22 September 2022; pp. 1–4.
10. Hu, Z.; Zhao, C.; Chen, Y.; Zhang, M.; Chen, J.; Li, W.; Zhao, L.; Tang, M. Enabling endogenous DAS in P2MP digital subcarrier coherent transmission system with enhanced frequency response. In Proceedings of the 2024 Optical Fiber Communications Conference and Exhibition (OFC), San Diego, CA, USA, 24–28 September 2024; pp. 1–3.
11. Wang, Y.; Huangfu, S.; Gao, H.; Wang, J.; Qiu, J.; Gui, X.; Fu, X.; Li, Z. Integrated design of an anti-polarization-fading UWFBG distributed acoustic sensing system. *Opt. Lett.* **2026**, *51*, 1243–1246. [CrossRef] [PubMed]
12. Wang, H.; Zhai, T.; Wang, Y.; Liu, Y.; Zhou, R.; Peng, X.; Zhang, Z. Real-time sensing approach for optical frequency domain reflectometry using an FPGA-based high-speed demodulation algorithm. *Opt. Express* **2024**, *32*, 33247–33261. [CrossRef] [PubMed]
13. Boitier, F.; Lemaire, V.; Pesic, J.; Chavarria, L.; Layec, P.; Bigo, S.; Dutisseuil, E. Proactive Fiber Damage Detection in Real-time Coherent Receiver. In Proceedings of the 2017 European Conference on Optical Communication (ECOC), Gothenburg, Sweden, 17–21 September 2017; pp. 1–3.
14. Minelli, L.; Pellegrini, S.; Andrenacci, L.; Pilori, D.; Bosco, G.; Chiesa, L.D.; Tanzi, A.; Crognale, C.; Gaudino, R. SOP-based DSP blind anomaly detection for sensing on deployed metropolitan fibers. In Proceedings of the 49th European Conference on Optical Communications (ECOC 2023), Glasgow, UK, 1–5 October 2023; Volume 2023, pp. 519–522.
15. Yang, B.; Tang, J.; Zhuo, Q.; Hao, Y.; Fan, L.; Wang, S.; Gao, S.; Liang, J.; Hu, W.; Yao, Y.; et al. Robust SOP-Based Vibration Sensing Integrated in DSCM System Based on Frequency-Domain Pilot Tones. In *Proceedings of the Frontiers in Optics + Laser Science 2024 (FiO, LS)*; Optica Publishing Group: Washington, DC, USA, 2024; p. FD1.6.
16. Yang, B.; Tang, J.; Cheng, C.; Fan, L.; Yang, P.; Wang, S.; Zhao, T.; Liang, J.; Gao, S.; Wei, J.; et al. Integrated communication and enhanced forward phase-based sensing based on frequency-domain pilot tones in DSCM systems using 100 kHz ECLs. *J. Light. Technol.* **2025**, *43*, 2664–2671. [CrossRef]
17. Mazur, M.; Fontaine, N.K.; Kelleher, M.; Kamalov, V.; Ryf, R.; Dallachiesa, L.; Chen, H.; Neilson, D.T.; Quinlan, F. Continuous distributed phase and polarization monitoring of trans-atlantic submarine fiber optic cable. In Proceedings of the 2024 Optical Fiber Communications Conference and Exhibition (OFC), San Diego, CA, USA, 24–28 September 2024; pp. 1–3.

18. Andrenacci, L.; Pilori, D.; Pellegrini, S.; Minelli, L.; Bosco, G.; Crognale, C.; Piciaccia, S.; Gaudino, R. Comparison between Phase and Polarization Sensing using Coherent Transceivers over Deployed Metro Fibers. In Proceedings of the 2024 Optical Fiber Communications Conference and Exhibition (OFC), San Diego, CA, USA, 24–28 September 2024; pp. 1–3.
19. Sadighi, L.; Karlsson, S.; Natalino, C.; Furdek, M. Machine learning-based polarization signature analysis for detection and categorization of eavesdropping and harmful events. In Proceedings of the 2024 Optical Fiber Communications Conference and Exhibition (OFC), San Diego, CA, USA, 24–28 September 2024; pp. 1–3.
20. Virgillito, E.; Straullu, S.; Aquilino, F.; Bratovich, R.; Awad, H.; Proietti, R.; D'Amico, A.; Pastorelli, R.; Curri, V. Detection, Localization and Emulation of Environmental Activities Using SOP Monitoring of IMDD Optical Data Channels. In *Proceedings of the 2023 23rd International Conference on Transparent Optical Networks (ICTON), Bucharest, Romania, 2–6 July 2023*; IEEE: New York, NY, USA, 2023; pp. 1–4.
21. Chen, M.; Rao, X.; Liu, K.; Wang, Y.; Chen, S.; Xu, L.; Xu, R.; Chen, G.Y.; Wang, Y. Distributed Vibration Sensing Based on a Forward Transmission Polarization-Generated Carrier. *Sensors* **2024**, *24*, 5257. [CrossRef] [PubMed]
22. Skarvang, K.S.Y.; Bjørnstad, S.; Sæthre, E.; Hjelme, D.R. Local wind impact sensing using state of polarization measurement on a live short-haul aerial fibre cable. In *Proceedings of the Optical Fiber Communication Conference*; Optica Publishing Group: Washington, DC, USA, 2024; p. Tu2J-5.
23. Straullu, S.; Aquilino, F.; Bratovich, R.; Rodriguez, F.M.; D'Amico, A.; Virgillito, E.; Pastorelli, R.; Curri, V. Real-time Detection of Anthropic Events by 10G Channels in Metro Network Segments. In Proceedings of the 2022 IEEE Photonics Conference (IPC), Vancouver, BC, USA, 13–17 November 2022; pp. 1–2.
24. Notarstefano, F.; Clivati, C.; Donadello, S.; Virgillito, E.; Bratovich, R.; Corsini, R.; Hovsepyan, M.; Carpentieri, F.; Curri, V. Multi-tech Sensing on Live Telecom Fiber: Comparing Phase and State-of-Polarization for Cable-Safety Monitoring. In *Proceedings of the Optical Fiber Communication Conference*; Optica Publishing Group: Washington, DC, USA, 2026; p. M4J-3.
25. Yang, B.; Yu, H.; Yan, Y.; Zhang, C.; Tang, J.; Hao, Y.; Wei, J.; Sun, G.; Yang, Y. Accurate vibration recognition enabled by synergistic sensing based on both phase and SOP for stable IM-DD optical interconnects. *J. Opt. Commun. Netw.* **2026**, *18*, B85–B96. [CrossRef]
26. Hecht, E. *Optics*, 5th ed.; Pearson: Boston, MA, USA, 2017.
27. Fang, X.; Zhu, Y.; Zhou, L.; Li, Y.; Yang, C.; Zhou, X.; Hu, W.; He, Z.; Wang, L.; Li, K.; et al. 1.2-Tb/s/λ IM/DD Optical Interconnects with Stokes Vector Receiver. In Proceedings of the 2024 Asia Communications and Photonics Conference (ACP) and International Conference on Information Photonics and Optical Communications (IPOC), Beijing, China, 2–5 November 2024; pp. 1–5.
28. Spammer, S.J.; Swart, P.L.; Booysen, A. Interferometric distributed optical-fiber sensor. *Appl. Opt.* **1996**, *35*, 4522–4525. [CrossRef] [PubMed]
29. Brown, D.A. A symmetric 3x3 coupler based demodulator for fiber optic interferometric sensors. In *Proceedings of the Fiber Optic and Laser Sensors IX*; DePaula, R.P., Udd, E., Eds.; SPIE: Bellingham, WA, USA, 1991; Volume 1584, p. 328.
30. Frosio, G.; Dändliker, R. Reciprocal reflection interferometer for a fiber-optic Faraday current sensor. *Appl. Opt.* **1994**, *33*, 6111–6122. [CrossRef] [PubMed]
31. Yin, K.; Zhang, M.; Ding, T.; Wang, L.; Liao, Y. Research on an improved passive demodulation method for optical fiber interferometer with 3x3 coupler. In *Proceedings of the Fundamental Problems of Optoelectronics and Microelectronics III*; Kulchin, Y.N., Ou, J., Vitrik, O.B., Zhou, Z., Eds.; International Society for Optics and Photonics SPIE: Bellingham, WA, USA, 2007; Volume 6595, p. 65954B.
32. Tang, J.; Yang, B.; Wei, J.; Cheng, C.; Hao, Y.; Wu, Q.; Wang, J.; Liang, J.; Xu, Z.; Sun, Z.; et al. Low-complexity and Multiplier-free Baud-rate Timing Phase Error Detector for high-speed optical IM/DD Systems. In *Proceedings of the 2024 Conference on Lasers and Electro-Optics Pacific Rim (CLEO-PR)*; Optica Publishing Group: Washington, DC, USA, 2024; p. P2-088.
33. Tang, J.; Li, Y.; Cheng, C.; Wang, X.; Yang, B.; Liang, J.; Xu, Z.; Fan, L.; Sun, Z.; Hu, W.; et al. Beyond 100-Gbps IM/DD Optical Interconnects at 2-Micron Waveband Under Severe Bandwidth Limitation Enabled by Advanced DSP. *J. Light. Technol.* **2025**, *43*, 8657–8665. [CrossRef]
34. Boitier, F.; Layec, P.; Polo, F.; Nale, A.; Lonardi, M.; Costantini, C.; Belzner, M.; Posilovic, R.; Benz, A.; Eggers, D.; et al. Advancing SOP Event Localization through Commercial Transponder Characterization. In *Proceedings of the Optical Fiber Communication Conference*; Optica Publishing Group: Washington, DC, USA, 2026; p. Tu2A-4.
35. Zhang, J.; Qiao, G.; Zuo, M.; Yang, Y.; Wang, Y.; Long, C.; Chen, Z.; He, Y.; Li, J. Unidirectional integrated vibration sensing and communication based on weakly-coupled FMF. *Opt. Commun.* **2025**, *597*, 132601. [CrossRef]

Disclaimer/Publisher's Note: The statements, opinions and data contained in all publications are solely those of the individual author(s) and contributor(s) and not of MDPI and/or the editor(s). MDPI and/or the editor(s) disclaim responsibility for any injury to people or property resulting from any ideas, methods, instructions or products referred to in the content.